Numerical Method for Estimation of Propeller Efficiencies

U. P. Solies*
University of Tennessee Space Institute, Tullahoma, Tennessee 37388

Nomenclature

A = propulsive disk area, $\pi D^2/4$
C_p = power coefficient, $P/(\rho n^3 D^5)$
D = propeller diameter
J = advance ratio
M = Mach number
P = power at the propeller shaft
q = dynamic pressure
T = thrust
V = velocity
ΔV = propeller slipstream velocity
η = propulsive or propeller efficiency
ρ = freestream air density

Introduction

DURING the conceptual design and preliminary performance analysis of propeller aircraft, frequently the propulsive efficiency and the corresponding thrust must be determined at various speeds. For a given engine power and propeller diameter, for example, the thrust variation with airspeed is required for the calculation of takeoff distance, climb performance, cruising speed, and maximum level flight velocity.

Typically at this point the designer is interested in a simple and quick method that yields reasonably accurate results which can be used for parametrical studies of aircraft performance, assuming that an optimized propeller design will be found later in the process. In this context, absolute accuracy is not as important as consistency, relative simplicity, and the ability to show proper trends. The algorithm presented below was developed for these purposes and can easily be programmed.

Theory

The following equations were derived from air vehicle performance and momentum considerations for a propulsive disk[1]:

$$\eta = \eta_0 \eta_i \tag{1}$$

$$T = (\eta P/V) \tag{2}$$

$$(\Delta V/2) = -(V/2) + \sqrt{(V^2/4) + (T/2\rho A)} \tag{3}$$

$$\eta_i = \frac{V}{V + (\Delta V/2)} \tag{4}$$

Equation (1) describes η as the product of profile efficiency η_0 and induced or ideal efficiency η_i, Eq. (4). V is the vehicle's velocity and equals that of the relative wind several prop diameters ahead of the propeller. $V + \Delta V$ is the velocity of the air in the propeller slipstream several prop diameters behind the propeller. It can be shown[2] that the velocity at the propeller disk is $V + \Delta V/2$.

Equation (2) expresses the thrust developed by the propeller, with P being the power generated by the engine at the propeller shaft. Since the thrust is inversely proportional to velocity, it increases with decreasing speed, however, at lower speeds the propulsive efficiency decreases also. Inspection of Eq. (4) reveals that the ideal propulsive efficiency becomes zero at zero velocity, indicating the fact that the aircraft is not propelled ($V = 0$), and all the shaft power is converted into the flow of kinetic energy in the slipstream. Conversely, at high speeds the ideal efficiency approaches unity since the slipstream velocity decreases, Eq. (3). This behavior of η_i is shown as curve "a" in Fig. 1 and represents the theoretical maximum for η.

The thrust usually peaks at the static condition, where η and V are both zero. Equation (2) becomes therefore meaningless, however, it can be shown[2] that at the limit $V \to 0$ the static thrust becomes

$$T_s = (2\rho A)^{1/3}(\eta_0 P)^{2/3} \tag{5}$$

Because the propulsive disk analysis ignores effects of air viscosity, compressibility, and slipstream rotation, the propeller efficiency η is smaller than η_i. This is expressed in Eq. (1) by the profile efficiency η_0, which accounts for friction, downwash, partial flow separation, and compressibility effects at the propeller blades. The profile efficiency reaches a maximum at the design advance ratio J_{des}, where propeller design parameters such as the distribution of local angles of attack along the radius are optimized. For a given engine speed, this occurs at the design velocity V_{des}.

At off-design velocities the profile efficiency is smaller, since the blade twist is no longer optimal and other factors affect the propeller performance unfavorably. This is true for both variable and fixed pitch propellers, even though for the variable pitch propeller the profile efficiency varies much less and remains near the optimum for a wide range of velocities in the climb and cruise range. At high speeds, it drops off due to transonic effects at the propeller tips. For fixed pitch props, the profile efficiency drops off rapidly to both sides of the design speed, due to unfavorable changes in blade angles of attack. Figure 1 shows typical propulsive efficiencies of the idealized momentum disk ($\eta_0 = 1.0$), a variable pitch "con-

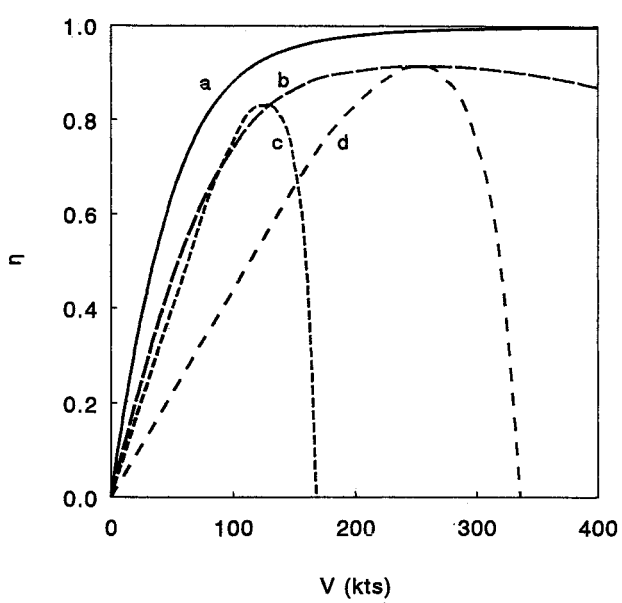

Fig. 1 Typical variation of propulsive efficiencies vs airspeed for different devices: a—momentum disk (theoretical maximum); b—constant speed propeller (variable pitch); c—climb prop (fine pitch, fixed); and d—cruise prop (coarse pitch, fixed). P = 300 hp and D = 6.83 ft.

Received May 2, 1993; revision received May 20, 1993; accepted for publication July 21, 1993.

*Assistant Professor, Departments of Aviation Systems and Aerospace Engineering, M/S-01. Member AIAA.

stant speed" propeller, a fixed pitch cruise prop (high pitch), and a fixed pitch climb prop (low pitch), all of same diameter.

In summary, Eqs. (1–5) contain 10 variables, four of which are known, namely P, V, ρ, and A, and six are unknown, namely ΔV, T, T_s, η, η_i, and η_0. To make the system solvable, a sixth equation was added:

$$\eta_0 = \text{const} \tag{6}$$

This represents an approximation for the profile efficiency of a constant speed propeller at climb and cruising speeds, or for the profile efficiency of a fixed pitch propeller at and near its design speed. The choice of the constant in Eq. (6) is empirical: it depends on the class of propellers considered, and requires some engineering judgement. Since η_i approaches unity at high speeds

$$\eta_0 \approx \eta_{\text{exp}} \tag{7}$$

where η_{exp} is an average of experimental data for propulsive efficiencies near design cruise speeds for typical propellers of the type considered. More accurately, η_0 can be determined by inserting η_{exp} into Eq. (2), proceeding with Eqs. (3) and (4), and then solving Eq. (1) for η_0.

Reference 3 shows peak efficiencies of three-bladed propellers used for modern light and business aircraft ranging from 0.83 to 0.92, obtainable at advance ratios between 1.1–2.6 and power coefficients between 0.03–0.33. For propellers operating outside these ranges, the peak efficiency drops off. This must be considered in estimating η_0.

Raymer[4] suggests increasing the cruise efficiency by 3% for two-bladed propellers, and reducing it by 10% for wooden propellers, due to thicker airfoils.

The propellers with the higher cruise efficiencies typically offer less thrust at static conditions and low speeds. These and other performance characteristics of specific propellers depend on additional parameters, such as activity factors and design lift coefficients of the propeller blades, which have to be chosen by the designer and go beyond the scope of the method presented here.

At some point, any serious design effort usually incorporates actual propeller performance data, as available from propeller manufacturers for a selected propeller design. These include variations of η_0, e.g., at very low speeds due to flow separation at the inner portions of the propeller blades (typically for $V < 0.3V_{\text{des}}$), and at high speeds due to the transonic drag rise at the tips (typically for $M_{\text{tip}} > 0.9$).

The assumption $\eta_0 = \text{const}$ is a meaningful simplification for constant speed propellers in the context of conceptual design, where the emphasis is on variation of aircraft design parameters and the study of basic trends. For fixed pitch propellers, η_0 can no longer be assumed to be constant over a wide speed range. Assuming that a well designed propeller will be found later, the method can still be used to predict an envelope of propeller efficiencies at various design speeds. Raymer[4] suggests a graphical method that permits estimation of the ratio η/η_{des} as a function of J/J_{des}.

Example

To determine the propulsive efficiency for a given engine, propeller diameter, and speed, one can proceed as follows: 1) guess a first value of η; 2) compute T, Eq. (2); 3) compute $\Delta V/2$, Eq. (3); 4) compute η_i, Eq. (4); 5) with η_0 estimated, Eq. (5), get a refined value for η from Eq. (1); and 6) repeat steps 2–5 until η has sufficiently converged.

The iteration is stable and converges rapidly, even if the initial guess for η is far off. A numerical example with P = 300 hp, D = 6.83 ft, V = 50 kt, η_0 = 0.9, and ρ = 0.002377 slugs/ft^3 is shown in Table 1.

The procedure can be repeated for other velocities, and a diagram of T and η vs V can be established. The result for the above example is shown as curve "b" in Fig. 2. Curve "a" shows the same example with η_0 = 1.0, showing the theoretical maximum for this propeller diameter and shaft power.

Table 1 Sample iteration

Iteration,	η,	T, lb	$\Delta V/2$, ft/s	η_i,	η,
0	0.9000	1760	66.82	0.5581	0.5023
1	0.5023	982	43.94	0.6576	0.5919
2	0.5919	1157	49.59	0.6299	0.5669
3	0.5669	1108	48.05	0.6372	0.5735
4	0.5735	1121	48.46	0.6352	0.5717
5	0.5717	1118	48.35	0.6358	0.5722
6	0.5722	1119	48.38	0.6356	0.5721
7	0.5721	1118	48.37	0.6357	0.5721

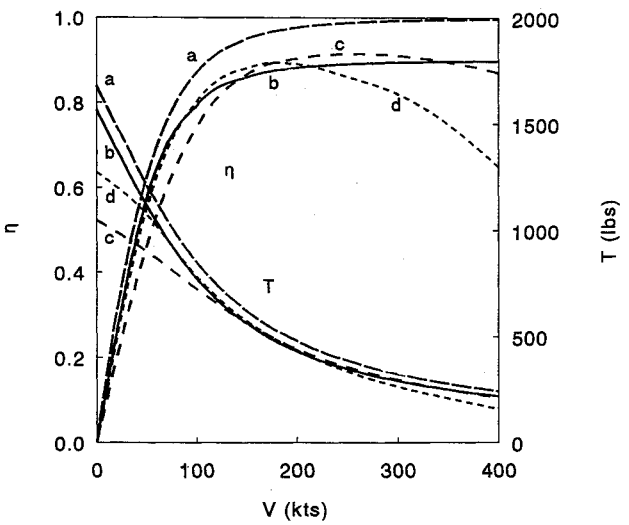

Fig. 2 Propulsive efficiency and thrust vs airspeed. Comparison of results obtained by semi-empirical numerical method with results obtained from propeller performance charts[3]: a—numerical method with η_0 = 1.0 (theoretical maximum); b—numerical method with η_0 = 0.9; c—propeller with low design lift coefficient ($C_{L\text{des}}$ = 0.15, AF = 80, C_p = 0.051); and d—propeller with high design lift coefficient ($C_{L\text{des}}$ = 0.50, AF = 80, C_p = 0.051). P = 300 hp and D = 6.83 ft.

For comparison, actual propeller performance data of two propellers[3] with the same diameter and shaft power are shown. Both have three blades with an activity factor of 80. At an engine speed of 2700 rpm, they operate with a power coefficient of C_p = 0.05125. Propeller "c" has an integrated design lift coefficient of C_{Li} = 0.15, which calls for thin airfoils with low drag at low angles of attack, but early flow separation at moderately high angles of attack. This explains the shape of the curve, providing high efficiencies at high speeds, but poor static and low speed thrust. Propeller "d" has a C_{Li} = 0.5 and thicker blade sections, providing better static thrust and low speed performance, but also an earlier efficiency dropoff at high speeds.

Conclusions

The shown algorithm is relatively simple, easy to program, and converges quickly. Its semi-empirical nature requires an educated choice of the profile efficiency η_0 at the design point. With a properly chosen η_0 it produces results that agree well with actual propeller performance data, except at the low and high speed end of the spectrum. While it cannot predict the effects of flow separation at low speeds and transonic effects at the propeller tips at high speeds, it does properly predict induced effects due to variation in disk loading and airspeed. Combining simplicity with generality, the method is particularly useful in the context of conceptual design.

References

[1]Nicolai, L. M., *Fundamentals of Aircraft Design*, METS, Inc., San Jose, CA, 1975, pp. 18-2–18-5.

[2]McCormick, B. W., *Aerodynamics, Aeronautics, and Flight Mechanics*, Wiley, New York, 1979, pp. 344–346.

[3]Anon., "Generalized Method of Propeller Performance Estimation," United Aircraft Corp., Hamilton Standard Rept. PDB 6101A, Windsor Locks, CT, 1963.

[4]Raymer, D. P., *Aircraft Design: A Conceptual Approach*, AIAA Education Series, AIAA, Washington, DC, 1989, pp. 325–330.

Experimental Investigation of Vortex Breakdown over a Sideslipping Canard-Configured Aircraft Model

Sheshagiri K. Hebbar* and Max F. Platzer†
Naval Postgraduate School,
Monterey, California 93943
and
Chang Ho Kim‡
Korean Air Force, Republic of Korea

Introduction

ALTHOUGH vortical flows dominate, the phenomenon of vortex breakdown (burst) and the onset of vortex asymmetry severely limit the high angle-of-attack (AOA) aerodynamics. When bursting is symmetric, only pitch stability is affected. When sideslip is present, the bursting becomes asymmetric, causing a rolling moment which adversely affects both roll and yaw stability. The effect of AOA on vortex bursting has been investigated extensively on delta wings,[1] and to a limited extent on complete aircraft configurations.[2–4] However, experimental data on the influence of sideslip on vortex bursting is limited,[5–7] and data on the effects of sideslip rate are still rather scarce even for simple wing shapes, let alone for complete aircraft configurations.

The canards affect the vortex development and have a strong influence on the lateral and directional stability.[8] The use of a close-coupled canard-configuration to achieve maneuverability and control in the poststall regime is the subject of growing scientific interest. Of special importance is the understanding of the vortex development and breakdown (bursting) under rapidly maneuvering conditions as envisioned for the U.S. Navy's X-31A aircraft. Therefore, an extensive, dye-injection flow-visualization study was undertaken in the Naval Postgraduate School (NPS) water tunnel, to characterize the vortical flowfield around a maneuvering canard-configured fighter aircraft model comparable to X-31A. The influence of canard location and pitch rate has been investigated earlier.[9,10] The results of the investigation on the effect of rate of sideslip are presented here. These *first* of a kind flow visualization results should be of interest to researchers working on similar configurations, especially in view of the clean support system used (Fig. 1). Additional details of the investigation appear in Refs. 11 and 12.

Received April 3, 1993; revision received June 21, 1993; accepted for publication July 6, 1993. This paper is declared a work of the U.S. Government and is not subject to copyright protection in the United States.

*Adjunct Professor, Department of Aeronautics and Astronautics. Associate Fellow AIAA.

†Professor, Department of Aeronautics and Astronautics. Associate Fellow AIAA.

‡Major.

Experimental Program

The NPS water tunnel is a horizontal, continuous flow, closed circuit facility with a test section 38 cm wide, 51 cm high, and 152 cm long. Water velocities of up to 30.5 cm/s are possible in the test section with a turbulence level of less than 1%. The dye-supply system for injecting color dyes through model ports consists of six pressurized color dyes using water soluble food coloring. The model support system, attached to the top of the test section, utilizes a C-strut to vary the pitch angle travel up to 50 deg, and a turntable to provide yaw variations up to ±20 deg (Fig. 1). Model pitch and yaw are controlled independently, with the yaw servo motor providing yaw rates of 1·8 deg/s and 2·8 deg/s.

The X-31A-like model used in this investigation is a simplified 2.3% scale model approximating the X-31A fighter aircraft with a double-delta wing, a delta-canard, a rectangular fuselage and several dye-injection ports (Fig. 2). The key dimensions of the model are: model length = 30.5 cm (12 in.), model span = 20.3 cm (8 in.), and wing root chord C_{wr} = 14.0 cm (5.5 in.). The canard's nondimensional location corresponded to $\bar{X}_c = X_c/C_{wr} = 43.18\%$, $\bar{Z}_c = Z_c/C_{wr} = 7.95\%$, where the canard's horizontal distance X_c and its vertical distance Z_c are measured from the quarter point of the canard root chord to the quarter point of the wing root chord.[10] The upper surface of the wing and the fuselage had grid lines marked for easy identification of vortex burst location.

The experimental program was carried out in two phases. The first phase involved the vortex flow visualization of the static model in the AOA range α = 15–50 deg at sideslip angles of β = 0, 5, 10, 15, and 20 deg. The second phase involved the dynamic vortex flow visualization of the sideslipping model for two rates of sideslip with β varying from 0 to 20 deg (simple sideslip increase motion) and 20 to 0 deg (simple sideslip decrease motion), both in the AOA range of 15 to 50 deg. The flow velocity in the water tunnel was nearly constant at 7.5 cm/s, corresponding to a nominal Reynolds number of 1.02×10^4 based on the wing root chord. The reduced yaw rates were $\dot{\beta}b/2U_\infty = 0.05$ and 0.08, where b is the model span, U_∞ is the freestream velocity, and $\dot{\beta}$ is the sideslip rate in rad/s. Note that these rates are comparable with the flight value of 0.03 for an assumed sideslip rate of 40 deg/s at 150 kt. The model yaw-axis was located at 62.7% of the wing root chord (21.5 cm aft of the nose). Extensive videotape recording and 35-mm photography of the model flowfield in both top view and side view were performed to document the observed flow phenomena during static and dynamic conditions.

Results and Discussion

All measurements were made on the *leeward* side of the model. Data reduction essentially consisted of measuring the burst location of the wing root vortex X_b from the leading edge of the wing root chord and plotting it as a function of AOA. The burst locations were determined from the photographs with the utmost care and consistency, and scaled for nondimensionalization using the wing root chord. Where necessary, videotape playback was used for clarification/confirmation of vortex burst location. Some degree of imprecision may be present in the reduced data due to the difficulty in locating the burst point, particularly at high angles of attack combined with high-rate dynamic motion. In addition, during the static segment of the experiment the burst location at any AOA was unsteady and fluctuated up to ±0.63 cm (i.e., about 4.5% of the wing root chord) about the mean location. For a discussion on the quality of NPS water tunnel burst data, see Hebbar et al.[4]

Figure 3 shows a typical asymmetric wing root vortex flow pattern at 20-deg AOA and 5-deg sideslip angle, with the vortex bursting on the leeward side at 75% of the wing root chord and lagging that on the windward side. The sideslip